Advances in Geo-Energy Research

Vol. 14, No. 3, p. 224-237, 2024

Original article

Effects of end-member sediments on CO_2 hydrate formation: Implications for geological carbon storage

Shuang Cindy Cao[1], Yanli Yuan[1], Jongwon Jung[2], Hui Du[3], Xiaofang Lv[3], Xiaoshuang Li[1]*

[1]*School of Urban Construction, Changzhou University, Changzhou 213000, P. R. China*

[2]*School of Civil Engineering, Chungbuk National University, Chungbuk 28644, Korea*

[3]*School of Petroleum and Natural Gas Engineering, Changzhou University, Changzhou 213000, P. R. China*

Keywords:
Carbon sequestration
CO_2 hydrate
end-member sediments
nucleation sites
electrical sensitivity

Cited as:
Cao, S. C., Yuan, Y., Jung, J., Du, H., Lv, X., Li, X. Effects of end-member sediments on CO_2 hydrate formation: Implications for geological carbon storage. Advances in Geo-Energy Research, 2024, 14(3): 224-237. https://doi.org/10.46690/ager.2024.12.07

Abstract:
The conversion of CO_2 into solid hydrates for seabed storage is a promising greenhouse gas mitigation method, but the influence of reservoir types on hydrate formation remains unclear due to the complexity of marine sediments. This study examines three end-member sediments-montmorillonite, diatoms, and glass beads-representing clay-, silt-, and sand-dominated reservoirs, respectively. A series of kinetic experiments, morphological observations, and electrical sensitivity tests were conducted to assess the impact of these sediments on hydrate formation. The results show that the surface electric field and water migration properties of montmorillonite provide additional nucleation sites, promoting hydrate formation during the induction period. Gas consumption and hydrate conversion rate in the montmorillonite system were five times higher than those in the deionized water control group and ten times higher than those in the diatom and glass bead systems. While diatoms facilitated milder reactions in later stages, rapid hydrate formation in montmorillonite impeded further CO_2 mass transfer. Glass beads exhibited stringent formation conditions with Ostwald ripening effects. Hydrate films initially formed at the gas-liquid interface and spread into gas and water phases via surface tension-driven water migration. Electrical sensitivity tests revealed an inverse correlation between sensitivity and induction/reaction times across sediment types.

1. Introduction

Since the Industrial Revolution, activities such as fossil fuel combustion have dramatically increased CO_2 emissions. According to the Intergovernmental Panel on Climate Change (IPCC, 2007), CO_2 accounts for 55% of total greenhouse gas emissions (Wang et al., 2024), making it a major contributor to the greenhouse effect. As of 2022, global greenhouse gas emissions from energy production reached 41.3 billion tons, with CO_2 emissions exceeding 36.8 billion tons. In the same year, China's carbon emissions alone reached 11.6 billion tons (Wei et al., 2024). These excessive emissions exacerbate global warming, increasing the likelihood of severe ecological and social consequence (Ma et al., 2022; Feng et al., 2023). Recently, Carbon Capture, Utilization, and Storage (CCUS) technology has garnered significant attention as a means of addressing climate change and mitigating greenhouse gas emissions. The International Energy Agency projects that by 2060, 14% of the cumulative reduction in carbon emissions will come from CCUS technologies (Zhou and Abraham, 2018). Among the various strategies, carbon sequestration in deep seawater or seabed sediments through hydrate formation has attracted considerable interest (Hassanpouryouzband et al., 2019; Aminnaji et al., 2024). By 2021, more than 250 million tons of carbon had been sequestered in the ocean (Zhou and Abraham, 2018). The ocean's vast capacity-20 times greater than that of the terrestrial biosphere-makes it a critical player in CO_2 absorption (Schrag, 2009; Alhammad et al., 2023; Luo et al., 2023). However, challenges remain, such as the potential leakage of stored CO_2, leading to ocean acidification (Hönisch et al., 2012; Doney et al., 2020; Pandey et al., 2022).

*Corresponding author.
E-mail address: scaocindy@163.com (S. C. Cao); yuanyanli1113@163.com (Y. Yuan); jjung@chungbuk.ac.kr (J. Jung); huidu@cczu.edu.cn (H. Du); lvxiaofang5@cczu.edu.cn (X. Lv); scaocindy@cczu.edu.cn (X. Li).

Received October 19, 2024; revised November 12, 2024; accepted December 5, 2024; available online December 10, 2024.

Yandy Scientific Press

Table 1. Relevant studies on CO_2 marine storage methods, along with their associated advantages and limitations.

Method	Advantage	Key issue	Reference
Water column sealing	Easy to operate, no additional processing required	May cause seawater acidification	Sun et al. (2023); Ford et al. (2024)
Marine sediment storage	Generating stable carbonates with fast rate and high safety	High cost and cumbersome details	Eccles and Pratson (2012); Gislason and Oelkers (2014); Zhao et al. (2024)
Substitution method	Replacing natural gas to maintain seabed geological stability	Low replacement efficiency and high cost	Alhammad et al. (2024); Liu et al. (2024a)
Ocean fertilization	Utilizing plant photosynthesis with low input and high returns	Insufficient scientific support and basis	Bowie et al. (2001); Boyd and Abraham (2001); Buesseler et al. (2004)
CO_2 hydrate storage	Little impact on the marine environment, low risk of hydrate leakage	Crustal movement may cause cap rock to break	Luo et al. (2023); Zhao et al. (2024)

Hydrate-based carbon sequestration has emerged as a practical and effective solution (Ren et al., 2023). Prior studies on ocean storage have mainly focused on seabed marine storage methods, highlighting their advantages and limitations, as summarized in Table 1. Research has demonstrated that CO_2 hydrate formation occurs under relatively mild pressure and temperature conditions, with a high capacity for gas capacity and long-term stability (Wang et al., 2020; Qureshi et al., 2022). Therefore, the feasibility of underwater CO_2 containment is supported from a technical perspective (Ren et al., 2023).

According to the summary report by Zhang et al. (2023) on the composition of end-member (end-member composition refers to the extreme composition (i.e., may contain only one substance) of the mineral sequence arranged in purity) marine sediments worldwide, most marine hydrate reservoirs consist of clay, silt, and sand particles, although the proportion of each varies by region (Xia et al., 2023). In marine sediments, the proportion of clay minerals is relatively high, significantly influencing the generation and distribution of hydrates (Groos and Guggenheim, 2009; Schroeder et al., 2015). Analyses of reservoir samples in South China Sea indicate that the relative weight ratio of clay minerals in most areas is more than 20%. (Liu et al., 2010a, 2010b), with the core predominantly composed of montmorillonite, illite, and kaolin (Wu et al., 2018a), and a mass fraction reaching up to 30% (Li et al., 2018). In contrast, samples from SH-2 reveal a silt content as high as 70-80%. Meanwhile, core samples from the Nankai Trough, located off the central coast of Japan, show that the hydrate reservoir is primarily composed of coarse-grained sand layers (Ren et al., 2022). Some reservoirs consist of both clay and silt, which, togther with hydrates, play a structural role (Ren et al., 2022). Compared to silt and sand, clay minerals exhibit unique properties, including a small particle size ($< 5\ \mu$m), an excess of unbalanced negative charges on the surface, a large specific surface area (800 m^2/g), strong water adsorption capacity, and significant swelling potential (Cha et al., 1988; Martín-Puertas et al., 2007; Wu et al., 2018b). These characteristics can influence the kinetics of hydrate formation (Hubert et al., 2012). Park and Kwon, 2018 noted that the electric fields associated with clay particles promote the induced nucleation of hydrates. Montmorillonite, a dioctahedral 2:1 clay mineral, consists of two tetrahedral sheets flanked by a single octahedral sheet (Pecini and Avena, 2013; Li et al., 2020). Lee et al. (2002) reported that montmorillonite shortens the induction time for hydrate nucleation by offering additional nucleation sites, although it also shows down the kinetics of hydrate growth . Lamorena and Lee (2008) found that water adsorbed on the surface of bentonite and kaolin clay particles forms a hexagonal symmetric structure composed of oxygen and hydroxyl groups, which also affects the time required for hydrate formation. (Ren et al., 2023) Diatoms, which are photosynthetic microalgae and a type of silt particle, can enhance the formation of natural gas hydrates due to their larger pore spaces, allowing hydrates to develop at lower gas concentration levels (Jang et al., 2022). Bahk et al. (2013) demonstrated that the internal pores and nested structures of diatoms provide additional nucleation surfaces for hydrate formation (Bahk et al., 2013; Jang et al., 2022). Giovannetti et al. (2022) discovered that in the presence of small amounts of sodium chloride, sand particles can counteract the inhibitory effects of the salt. When the salt concentration is suitable, sand particles as porous media promote hydrate formation under mild thermodynamic conditions.

Although previous studies have explored the mechanisms through which various sediments influence hydrate formation, they lack a comprehensive comparison of the formation conditions and morphological characteristics across different end-member sediments. Furthermore, limited research has addressed the influence of geotechnical properties-such as liquid limit, plasticity, and electrical sensitivity-on hydrate formation. The sensitivity index of these sediments significantly impacts the geological and mechanical properties of the reservoir. (Sridharan and Nagaraj, 2000; Giovannetti et al., 2022). There is charge on the surface of end-member particles., combined with their varying electrical sensitivity indices, could lead to different responses to changes in pore fluid chemistry (Jang and Santamarina, 2016; Cao et al., 2019). These variations may alter the surface electric fields of the particles, thereby affecting the hydrate formation process. The electrical interac-

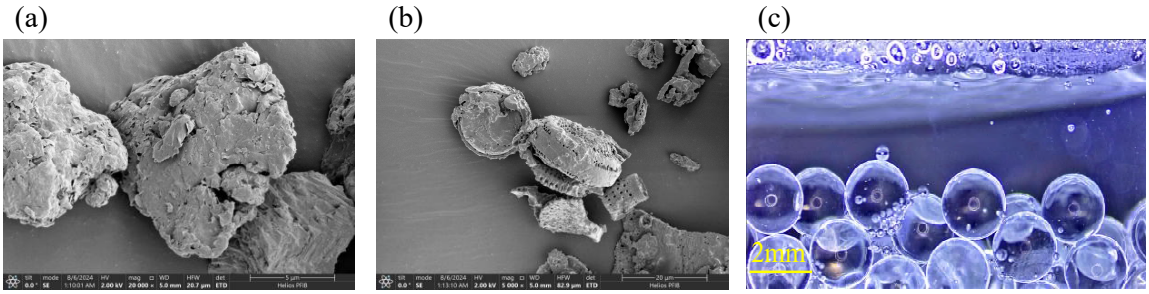

Fig. 1. SEM and micrograph images of end-member sediments. (a) Montmorillonite, (b) Diatom and (c) Glass beads.

Table 2. Basic indexes of the end-member sediments.

Sediments	Specific gravity[a)]	Median diameter (μm)	Specific surface area (m^2/g)
Glass beads	2.65	2,000[b)]	0.00015[c)]
Diatom	2.23	75[b)]	98[d)]
Montmorillonite	2.53	10.72[b)]	579[d)]

a) Density analysis by gas pycnometer (Jang et al., 2018), b) Data from manufacturer, c) Based on the calculation, d) Approximate value based on literature data (Jang et al., 2018)a

tions between particles involve attractive and repulsive forces. The Derjaguin-Landau-Verwey-Overbeek theory integrates van der Waals attraction and diffuse double-layer repulsion (DDL) (Butler, 1948; Derjaguin and Landau, 1993; Shackelford, 2005). Van der Waals forces result from short-range electrical interactions at distances of 10 nm or less (Valle-Delgado et al., 2005). The thickness of the DDL changes with ion concentration (Shackelford, 2005) (see Eq. (1)).

$$\vartheta \propto \sqrt{\frac{K}{C_0}} \tag{1}$$

where ϑ is the thickness of the DDL, C_0 is the diffusion ion concentration, K is the relative permittivity. This model suggests that pore fluid chemistry changes can affect particle interactions, leading to the formation of different clusters and fabrics among end-member sediments (Jang et al., 2018).

To effectively predict the electrical sensitivity of end-member sediments and its relationship to hydrate formation, it is necessary to evaluate the electrical sensitivity of various end-member sediments and correlate it with the hydrate formation process. This study, a series of experiments were carried out to study the kinetics and morphology of hydrate formation, systematically comparing the formation conditions and morphological evolution of hydrates across different end-member sediments. Montmorillonite, diatoms, and glass beads were selected to simulate end-member sediments composed mainly of clay, silt, and sand, thus, the geological conditions of hydrate reservoir are simulated more realistically. Glass beads were chosen over sand particles to enhance visualization during the experimental process, facilitating clearer observation of hydrate formation and its relationship with electrical sensitivity. This study systematically compares the effects of end-member sediments, representing clay, silt, and sand, on the kinetics and morphology of hydrate formation. The reactor was connected to a data acquisition system to monitor real-time temperature and pressure changes, enabling the calculation of differences in gas consumption, water-to-hydrate conversion rates, and hydrate formation induction time. High-speed camera and microscope were utilized to observe and analyze the growth patterns and morphology of hydrates within various end-member sediments. A combined liquid-plastic limit test was used to determine the boundary moisture content of the three end-member sediments, and the electrical sensitivity of each material was calculated to elucidate the relationship between hydrate formation and sediment properties, integrating previous research findings with electrical sensitivity analyses of the soil.

2. Experimental Methods

2.1 Materials

According to the characteristics of the actual marine gas hydrate accumulation area, the representative clay (montmorillonite), non-cohesive soil (diatom) and sand (SiO_2-glass beads) in the end-member minerals of the sediments commonly presented in hydrate reservoirs were selected. Montmorillonite (purity 96.2%, average particle size: 10.72 μm) was purchased from Shanlin Shiyu Mineral Products Co., Ltd.; diatom (purity $\geq$ 99.5%, average particle size: 75 μm) from West Asia Reagent Co.; and SiO_2-glass beads (diameter: 2,000 μm) from Quanzhou Precision Glass Bead Factory. CO_2 gas (purity 99.99%) was sourced from Huayang Gas Co., Ltd., while deionized water was produced in the laboratory. The Scanning Electron Microscope (SEM) analysis of the samples was performed on dried fine particles (Suzhou Chongyan Technology Co., Ltd., Tescan Mira4), with magnifications of 20,000 for montmorillonite and 5,000 for diatom. Table 2 summarizes the basic physical indexes of the end-member particulate matter used in this experiment. Fig. 1 summarizes the SEM and microscope images of the end-member particles used in this experiment.

2.2 CO_2 hydrate formation experiment

Device diagram of the experimental device is shown in Fig. 2. The reactor manufactured by Carbon and Carbon Technology Baoding Co., Ltd., is made of stainless steel

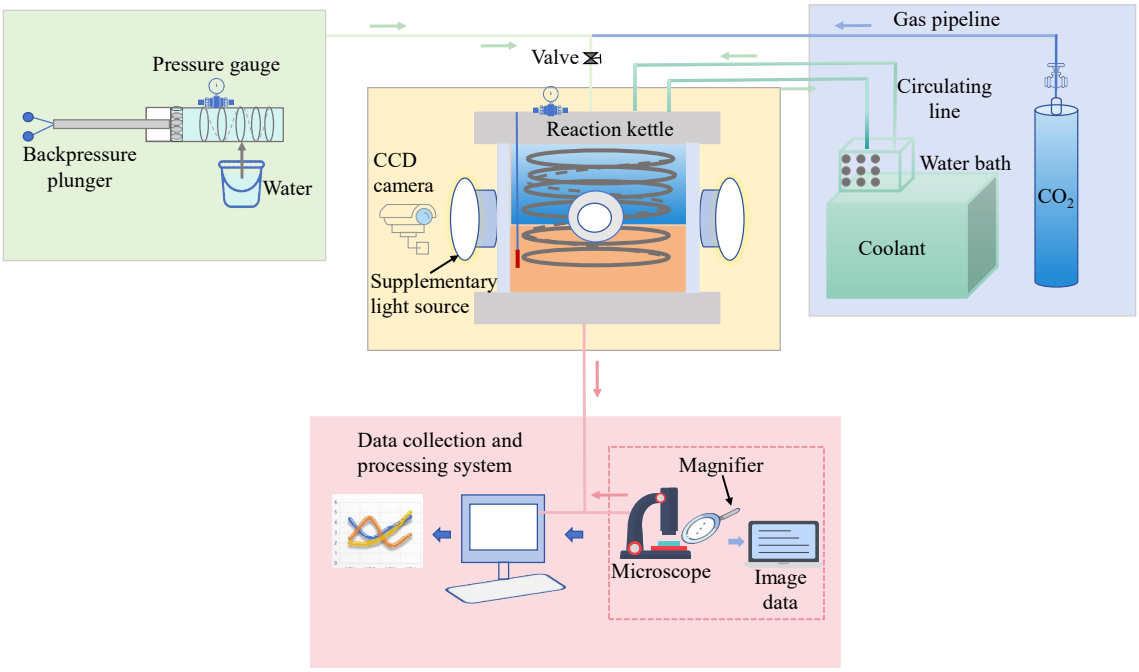

Fig. 2. Schematic of the visualized multifunctional reactor system.

with a maximum operating pressure of 30 MPa, a minimum temperature of -20 °C, and a volume of 1,500 mL (outer diameter 150 mm, inner diameter 120 mm, depth 150 mm). Four vision windows (diameter 3.5 cm, area 9.616 cm^2) are designed into the reactor to facilitate observation under different lighting conditions. These windows are equipped with sapphire lenses and bolted end caps to ensure high-pressure sealing. A CCD high-speed camera and microscope (Yanyue high-definition industrial microscope) were employed to monitor the macroscopic and microscopic morphology of CO_2 hydrate formation, decomposition, and sediments behavior. Pressure sensors (accuracy: 0.1 MPa) and temperature sensors (accuracy: 0.1 °C) were installed inside the reactor to record real-time data every 0.5 seconds.

First, a thorough airtightness test was conducted on the experimental pipeline system to ensure data accuracy. The experimental process is shown in Fig. 3.

Clean and dry the reaction vessel thoroughly. Prepare suspension of montmorillonite and diatom (> 100% saturation), stirred evenly and placed in a reaction vessel to ensure that the liquid level was aligned with the midpoint of the observation window (liquid level height 75-80 mm). For glass beads, clean them with deionized water, spread them into the reaction vessel, and added deionized water to the same liquid level height. Then the suspension was saturated with CO_2 at 2.5 MPa, and the temperature was stabilized at 15 °C using a water bath. The pressure in the reactor was increased again to 4 MPa and the temperature was reduced to 2 °C to induce hydrate formation. Hydrate formation is monitored by changes in pressure and temperature.

The mole number of gas consumed in the formation of CO_2 hydrate (Chen et al., 2019; Ma et al., 2022; Ren et al., 2023):

$$(\Delta n) = V\left(\frac{P}{ZRT}\right)_{t=0} - V\left(\frac{P}{ZRT}\right)_{t} \tag{2}$$

where Δn is the number of CO_2 gas moles consumed at time t. P is the pressure, T is the temperature, V is the gas volume, and Z is the gas compression coefficient, R is the ideal gas constant.

The reaction formula of CO_2 hydrate formation (Ma et al., 2022):

$$CO_2 + N \cdot H_2O \rightleftharpoons CO_2 \cdot \ N \cdot H_2O \tag{3}$$

where N is the hydration number, this study used a hydration value of 6.0, consistent with other studies (Zhang et al., 2020; Ma et al., 2022; Ren et al., 2023).

Water-to-hydrate conversion rate (C) (Chong et al., 2016; Ma et al., 2022):

$$C(\%) = \frac{(\Delta n)_{tf} \cdot N}{n_{H_2O}} \cdot 100\% \tag{4}$$

where $(\Delta n)_{tf}$ is the final number of moles consumed, and n_{H_2O} is the total amount of water.

2.3 Electrical sensitivity characterization

Electrical sensitivity is the ability of end-member sediments to respond to chemical changes in pore fluids based on liquid limits (L). (Jang and Santamarina, 2016, 2017; Jang et al., 2018). The liquid limit is measured using the boundary moisture content of deionized water (DW), 2 mol brine, and kerosene, designated as L_d, L_b, and L_k, respectively. The liquid limit, representing the boundary moisture content at which the sediment transitions from a plastic state to a liquid state under varying pore fluids (Shi et al., 2023), was determined using the standard cone penetrometer method (BS 1377, BSI 1990). The

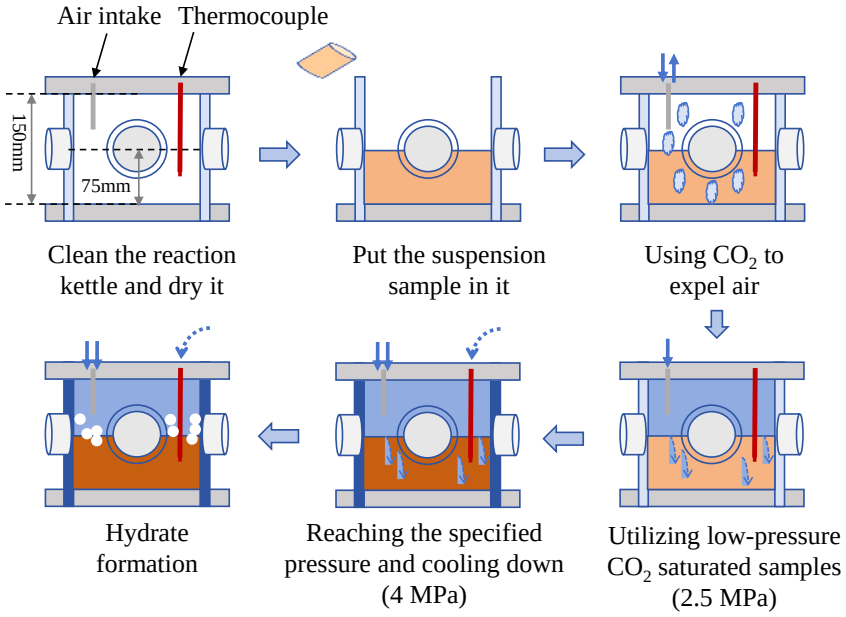

Fig. 3. Schematic diagram of hydrate formation experiment.

liquid plastic limit testing device (Shanghai Luda Experimental Instrument Co., Ltd., digital display soil liquid and plastic limit combined measuring instrument LP-100D) includes a cone meter, display screen, control switch, and sample cup. For the electrical sensitivity analysis, the calculation formula is as follows (Jang and Santamarina, 2016):

$$S_e = \sqrt{\left(\frac{L_d}{L_b} - 1\right)^2 + \left(\frac{L_k}{L_b} - 1\right)^2} \tag{5}$$

where L_d, L_b, and L_k represent the liquid limits measured in deionized water, saline water, and kerosene, respectively, indicating the boundary moisture content between the plastic and flow states of the soil.

Divide 200 g of each sample into three parts. Prepare three soil pastes for each sample with different water contents (near the liquid limit, near the plastic limit, or in between) using deionized water, 2 mol brine, and kerosene. Allow the pastes to stand in a moisture jar for 24 hours. Place each soil paste in the sample cup and level the surface. Position the sample cup on the digital display soil liquid and plastic limit combined measuring instrument's base for measurement. Measure the depth of the cone's penetration into the sample. After each measurement, extract at least 10 g of soil was taken into the oven for moisture content analysis.

3. Results and Discussion

3.1 Hydrate formation kinetics

3.1.1 Variations of temperature and pressure

This study used DW as a control to compare hydrate formation and decomposition behaviors in three end-member particulate materials under a driving pressure of 1.2 MPa. Temperature and pressure variations during CO_2 hydrate formation are shown in Fig. 4, highlighting the exothermic nature of hydrate nucleation (blue box), marked by a temperature rise and pressure drop (Li et al., 2024; Liu et al., 2024b). The time of the first visible hydrate particles was considered the induction nucleation time (Kvamme et al., 2020). Table 3 presents the detailed temporal, temperature, and pressure data from the four experimental setups, each performed under identical initial conditions. Compared with DW, the complete hydrate formation time of montmorillonite and diatom is shortened, and the time of glass beads is prolonged. Completion of hydrate formation was determined by a pressure change rate of less than 0.01 MPa/h. Fig. 5 visually summarizes the induction nucleation times in a bar chart format. Among the tested systems, DW exhibited the shortest induction time (75 s), followed by montmorillonite, diatom, and glass beads.

Montmorillonite, an expansive clay and a major constituent of marine sediments, carries unbalanced negative surface charges that attract cations in water, forming a double-layer electric field that reduces water activity. Compared with the deionized water system, the early formation of hydrate is inhibited, requiring higher pressure and lower temperature conditions for hydrate formation. However, due to its smaller particle size, montmorillonite presents a larger specific surface area and provides more nucleation sites for hydrate growth than other end-member sediments. As a result, it mitigates some of the inhibitory effects and moderately promotes hydrate formation (Bello-Palacios et al., 2021; Zhao et al., 2021; Ren et al., 2023).

The montmorillonite system had shorter induction and total hydrate formation times than the diatom and glass bead systems. Glass beads exhibited the longest times, with induction times 64, 19.2, and 8.1 times longer than those of deionized water, montmorillonite, and diatom, respectively (as shown in Table 3). This delay is attributed to their SiO_2 composition,

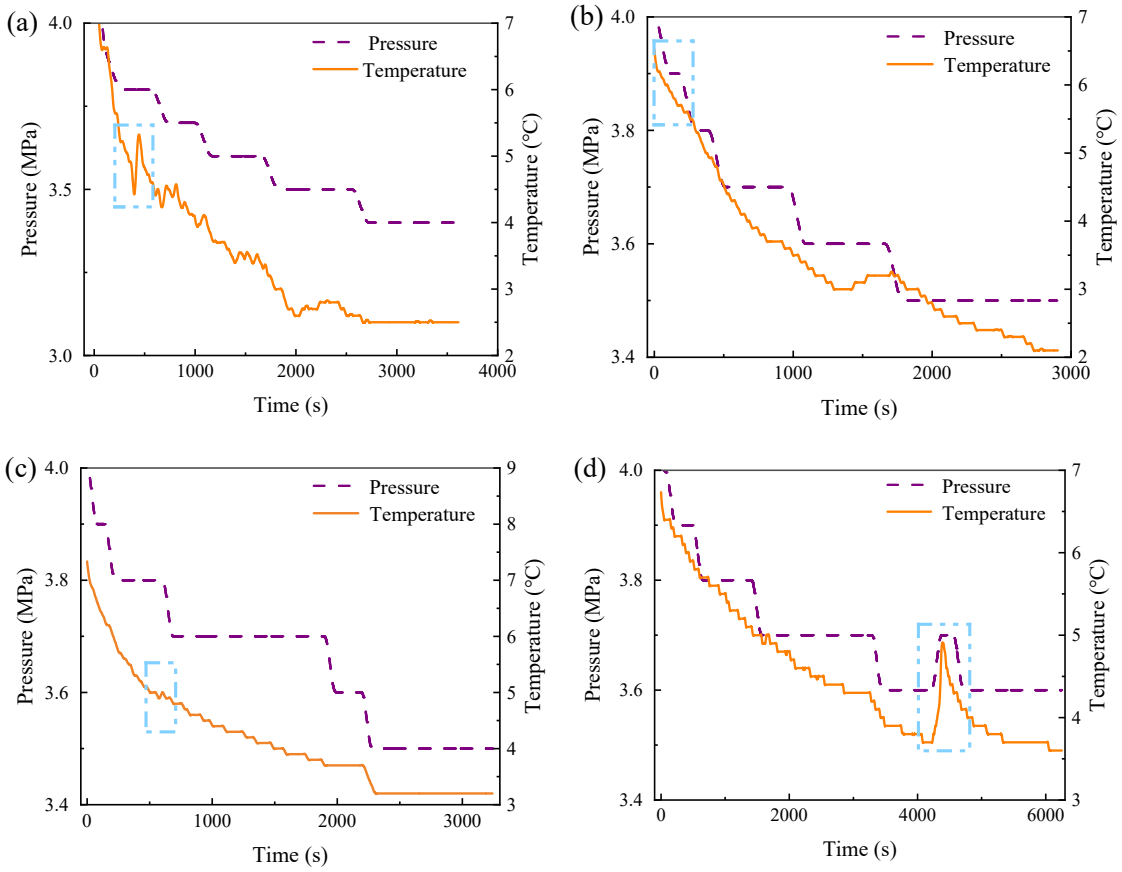

Fig. 4. Trends in temperature and pressure changes over time during the formation of hydrates. (a) DW, (b) montmorillonite, (c) diatom and (d) glass beads. (The blue dotted box represents the nucleation time for hydrates.)

Table 3. Comparison of temperature and pressure changes during hydrate formation.

Test	Initial condition			Hydrate appearance			Hydrate formation complete		
	t_0 (s)	P (MPa)	T (°C)	t_0 (s)	P (MPa)	T (°C)	t_0 (s)	P (MPa)	T (°C)
DW	0	4	7	75	4	6.5	3,600	3.4	2.4
Montmorillonite	0	4	7	250	3.9	5.6	2,900	3.5	2.1
Diatom	0	4	7	590	3.8	5	3,240	3.5	3.2
Glass bead	0	4	7	4,800	3.6	4	6,250	3.6	3.6

larger particle size, and reduced surface area, which inhibit gas diffusion and hydrate growth (Liu et al., 2023; Chen et al., 2024). Additionally, the 2 mm diameter of the glass beads, much larger than that of the other end-member particles, results in a reduced specific surface area, and the hydrate is in the form of surface cementation, which hinders the diffusion of gas and reduces the gas-liquid contact area, thus delaying the formation of hydrate.

3.1.2 Gas absorption and conversion rates

Montmorillonite had the highest gas consumption and conversion rate, nearly five times that of deionized water and ten times that of diatom and glass beads (as shown in Table 4). This is attributed to its smaller particle size, which increases the specific surface area and nucleation sites, and its surface electric field, which enhances gas-particle contact and promotes hydrate formation. In contrast, the glass beads exhibited the lowest gas consumption and conversion rate, likely due to the inhibitory effect of SiO_2 on hydrate formation (Liu et al., 2023; Chen et al., 2024).

3.1.3 Changes in pressure and temperature

The promoting effect of montmorillonite and diatom on hydrate formation occurs at different stages. Fig. 6 shows pressure and temperature trends during hydrate formation across the four experimental groups. In Region ①, montmorillonite required lower pressure than deionized water at the same temperature, indicating it facilitates hydrate formation under

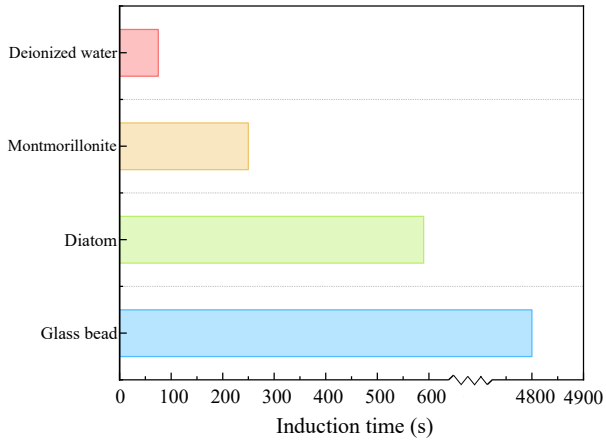

Fig. 5. Histograms of induction nucleation time for each experimental group.

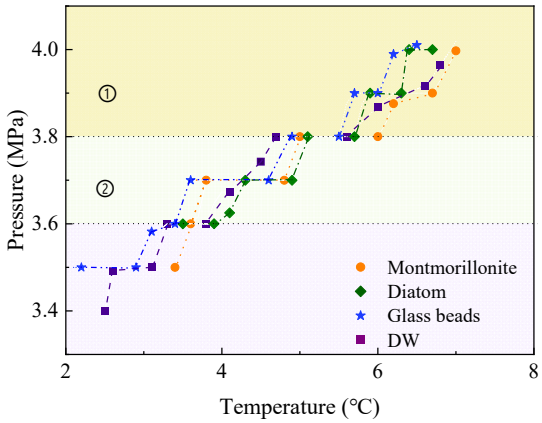

Fig. 6. Pressure variation trend with temperature during experimentation.

Table 4. Total gas consumption and water-to-hydrate conversion rate.

Test	Gas consumption (mol)	Conversion rate (%)
DW	0.6227	10.35
Montmorillonite	2.9377	48.81
Diatom	0.2955	4.91
Glass bead	0.2357	3.92

milder conditions. This is due to its ability to provide numerous nucleation sites, accelerating formation. Montmorillonite, composed of stacked mineral plates, interacts with surrounding water molecules, leading to adsorption. Previous research has shown that the adsorbed water molecules form hexagonal structures with oxygen and hydroxyl groups, mirroring montmorillonite's surface structure (Lamorena and Lee, 2008).

In Region ②, diatom displayed milder hydrate growth conditions at pressures below 3.8 MPa, benefiting from its small particle size and porous structure, which provide nucleation sites. However, the mass transfer limitations from high hydrate volumes become more prominent later, reducing hydrate formation. Hydrate formation increases the concentration of ions in the pore fluid, and the electrical sensitivity of diatom shows a relatively mild response, which leads to a decrease in the thickness of the diffusion double layer and results in sedimentation. The interaction between end-member fines and coarse particles provides a structural framework or attaches end-member particles to the surface of coarse particles, forming a sediment sealing unit encapsulated by hydrate. This may improve hydrate stability to some extent.

Glass beads required the harshest conditions, with longer induction and formation times due to cemented hydrates hindering mass transfer and their larger particle size. While SiO_2 in sand promotes hydrate growth at sizes below 0.46 mm, larger glass beads reduce the specific surface area, inhibiting formation (Mekala et al., 2014).

3.2 Hydrate morphology in end-member sediments

3.2.1 Morphological evolution

Under the same initial conditions (4 MPa, 7 °C), the growth morphology evolution of hydrates in different end-member sediments is also different. In the deionized water system (Fig. 7(a)), hydrates initially formed as thin films at the gas-liquid interface, expanding along the reactor wall and eventually penetrating both phases (t_0 represents the beginning of the experiment). This behavior aligns with Bai et al. (2020), who found that CO_2 hydrates preferentially form at the gas-liquid interface below the equilibrium temperature, forming a thin, stable film that thickens and ruptures as more hydrates accumulate. As CO_2 gas diffuses, this film gradually thickens and stabilizes until a substantial quantity of hydrates is generated, at which point the film ruptures and alters its stable state.

In systems with deionized water, montmorillonite, and diatom, hydrates also formed above the CO_2 phase (orange arrow in Fig. 7(a)). Although hydrates typically do not form in liquid CO_2, solid hydrates preferentially form due to surface tension, causing liquid water to migrate upward along the reactor wall and solid hydrate surface, creating a new gas-liquid interface and promoting further hydrate growth.

3.2.2 Micro-morphological evolution

As previous section mentined, Fig. 7(a) shows that montmorillonite significantly accelerates early-stage hydrate formation. In the 3.8 to 4.0 MPa range, hydrates rapidly form in montmorillonite, with all groups except the glass beads exhibiting substantial growth. Microscopic images (Fig. 7(b)) reveal hydrates in montmorillonite resembling those in deionized water, initially appearing as white filaments and later evolving into dense block-like structures. Fig. 8 further details this process, where hydrates first appear as bubbles (Fig. 8(a)) that coalesce into filaments and block-like structures. Arrows in Fig. 8(b) indicate that early hydrate growth involves clay and water migration due to small amounts of hydrate formation, creating new gas-liquid interfaces and enhancing growth (Ren et al., 2023). Additionally, the negatively charged montmoril-

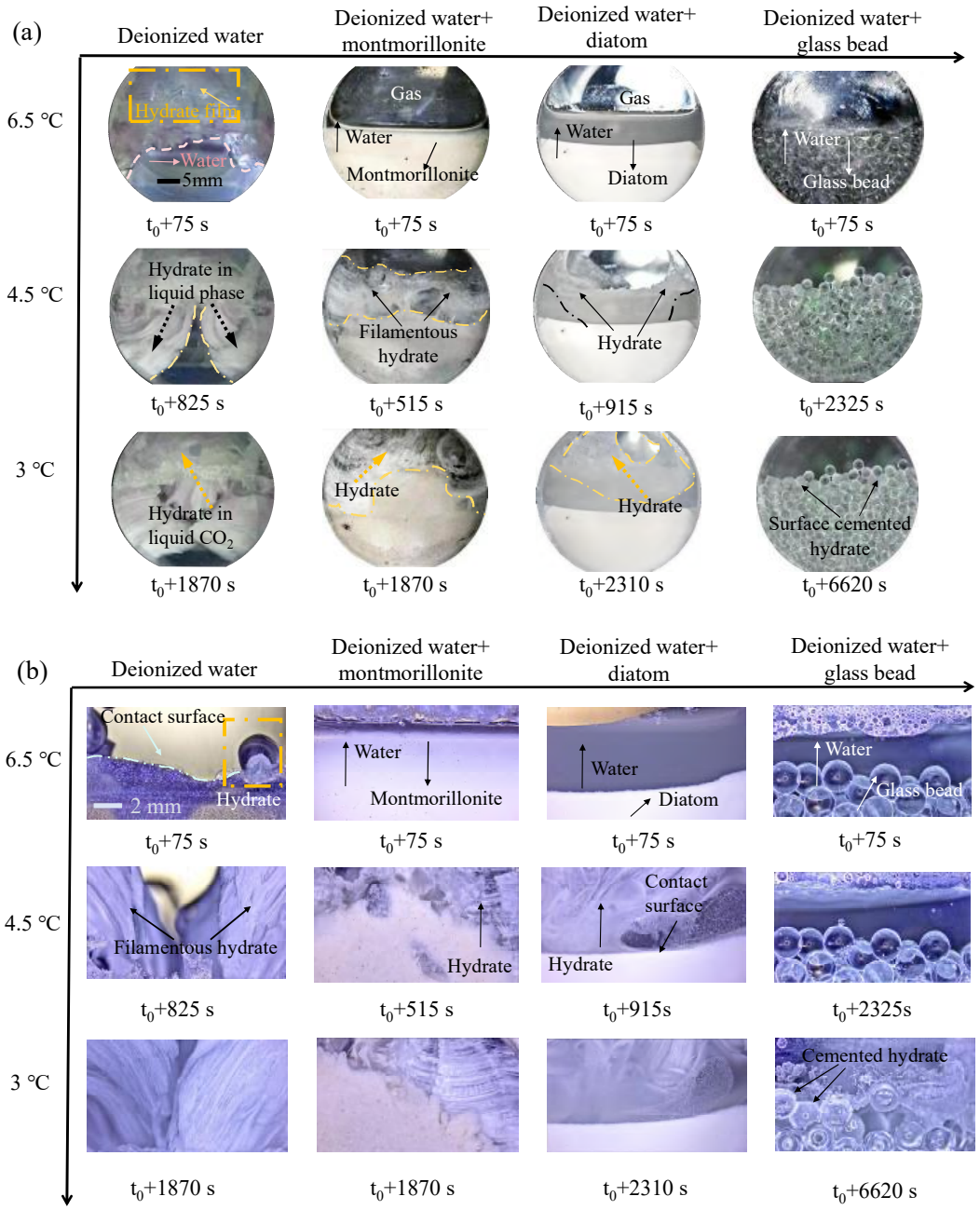

Fig. 7. The morphological evolution of hydrate formation process in different end-member sediments, including a longitudinal comparison within the same soil at the same pressure but different temperatures and a horizontal comparison across different soils under the same temperature and pressure. (a) Visual window images and (b) microscopic visible range images.

lonite particles interact with water and ions, forming a double-layer electric field that facilitates hydrate formation (Mojid and Cho, 2006). Higher pressures promote hydrate conversion (Sun et al., 2021), and small suspended particles can influence hydrate dynamics (Luckham and Rossi, 1999). The applied electric field also interacts with polarized water molecules, shortening the induction time (Park and Kwon, 2018).

Figs. 7 and 8 show that diatom and water undergo rapid stratification, with most diatom settling at the bottom. Due to diatom's non-cohesive nature, water absorption is limited. The morphology of hydrates in diatom differs from montmorillonite, appearing as milky white, ice-like structures with a relatively dense form. Fig. 8(c) show that hydrates initially form as bubble-like structures in a suspension with minimal particles, then extend downward into dense, block-like hydrates. The unique multi-hollow structure of diatom increases the specific surface area, providing additional nucleation sites and promoting hydrate formation.

The hydrate morphology in glass beads differs from other groups, with no prominent block-like structures (as shown in

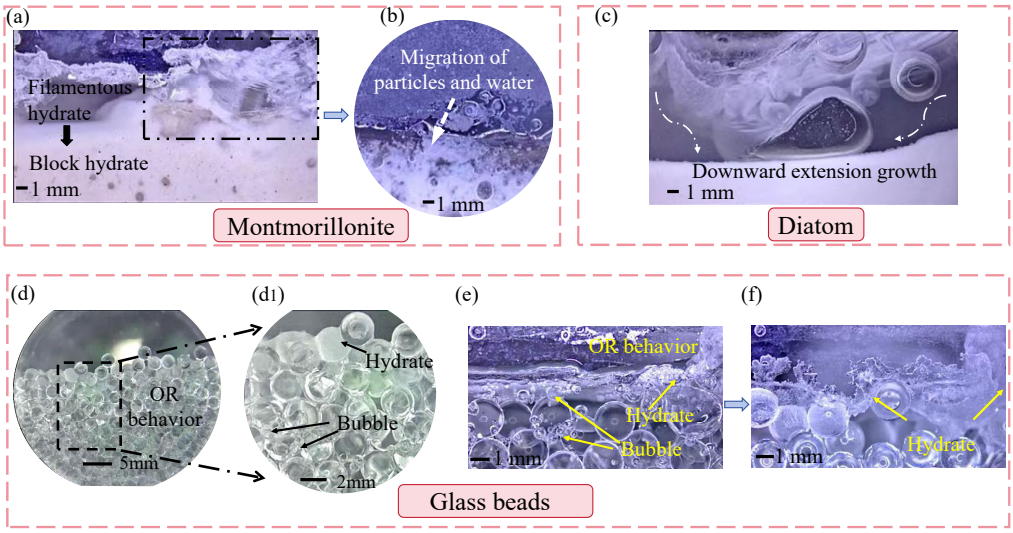

Fig. 8. Partial details of the hydrates formation process in montmorillonite , diatoms and glass beads. (a) Filamentous hydrates, (b) migration of particle-water , (c) initial bubbly hydrates, (d) OR behavior: dissolution of small particle hydrates, (d1) a locally enlarged image of (a), (e) the dissolution of small particle hydrates in OR behavior and (f) the OR behavior resulting in the generation of a large number of hydrates.

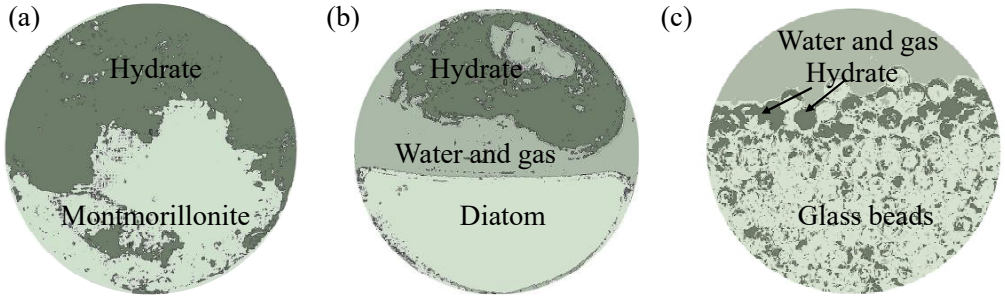

Fig. 9. The proportion of hydrate area in the visual range of the window. (a) The proportion of hydrate area in montmorillonite (54.62%), (b) the proportion of hydrate area in diatom (28.40%) and (c) the proportion of hydrate area in glass beads (6.91%).

Table 5. Area and proportion of hydrates within the visual window range.

Test	Hydrate area (cm^2)	Hydrate proportion (%)
Montmorillonite	5.252	54.62
Diatom	2.731	28.40
Glass bead	0.664	6.91

Fig. 8). Instead, hydrates form a bonded state between the glass beads. Bhattacharjee et al. (Bhattacharjee et al., 2015) found that hydrate formation occurs preferentially at the center of interparticle pores, rather than on the surfaces, which are more wetted by water than by gas. Significant Ostwald ripening (OR) behavior was also observed, where smaller hydrate particles dissolve due to their higher surface energy, and larger particles form as a result of supersaturation (Kong et al., 2017). This process, driven by energy release, is consistent with the presence of free water, which promotes further hydrate formation (Ren et al., 2023). Figs. 8(d), 8(e) and 8(f) show the dissolution of particles and the cemented state of the resulting hydrates. The OR behavior can enhance carbon sequestration by transforming unstable small hydrate particles into more stable large ones, reducing the risk of CO_2 gas leakage.

The proportion of final hydrates in different end-member sediments is different. Fig. 9 shows the proportion of hydrates in three end-member sediments, analyzed using ImageJ software. The dark green area represents hydrates, while green and light green represent end-member minerals and gas, respectively. This ratio reflects hydrates within the imaging window and not the entire reactor. Table 5 summarizes these proportions, with montmorillonite showing the highest hydrate area at 54.62%, followed by diatom at 28.4%, and glass beads at 6.9%.

In addition to the factors mentioned above, water saturation, mass fraction of sandy, clay, and silt components, internal pore structure, external electric fields, and organic matter in seawater can also influence hydrate formation and decomposition. Changes in resistance can verify gas absorption rates and temperature variations in sediment, allowing for analysis

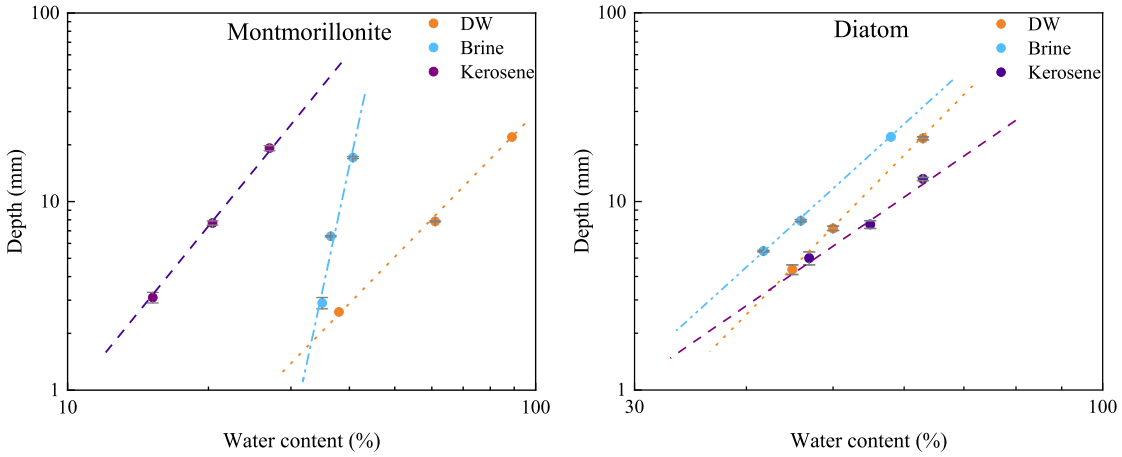

Fig. 10. Liquid and plastic limit data of diatom and montmorillonite in DW, brine, and kerosene.

Table 6. Liquid and plastic limits test results of end-member sediments.

Test	Liquid limit			Plastic limit	Plasticity index	Electrical sensitivity
	L_d	L_b	L_k			
Glass bead	0	0	0	0	0	Low
Diatom	61	53	65	39	22	Low
Montmorillonite	82	40	22	34	48	High

of hydrate formation rates and distribution across different locations. Subsequent experimental studies will explore the individual and combined effects of these factors to ensure that the findings align more closely with real-world conditions.

3.3 Electrical sensitivity and hydrate formation

To examine the effect of the electrical sensitivity of end-member sediments on hydrate formation, experiments were conducted to determine the boundary moisture content of three sediments. DW, 2 mol brine, and kerosene were used as pore fluids to assess the liquid limits and calculate electrical sensitivity. Note that glass beads, with a diameter of 2 mm, do not have a liquid limit and are not included in Table 6. A corrected liquid limit, accounting for the weight of the pore fluid, was applied in this study (Jang and Santamarina, 2016).

$$\left(\frac{L_k}{L_o}\right)_C = \frac{L_k}{L_b}\frac{1-C_b\frac{L_b}{100}}{G_k} \tag{6}$$

$$\left(\frac{L_d}{L_b}\right)_C = \frac{L_d}{L_b}\left(1-C_b\frac{L_b}{100}\right) \tag{7}$$

where subscript C represents the modified formula, G_k represents the specific gravity of kerosene, here 0.78 is used (from the manufacturer); C_b takes 0.1169.

The electrical sensitivity was calculated using Eqs. (5), (6) and (7), factoring in the specific gravity of kerosene (G_k) and the concentration of saline water (C_b). Table 6 presents the liquid limit, plastic limit, and electrical sensitivity index of the end-member sediments. Electrical sensitivity is categorized as low ($S_e < 0.4$), medium ($0.4 \leq S_e \leq 1$), or high ($S_e > 1$). Consistent with Jang and Santamarina (2016), montmorillonite shows high electrical sensitivity ($S_e > 1$), diatom exhibits low sensitivity ($S_e < 0.4$), and glass beads, with no liquid limit, are excluded from calculations. The sensitivity index indicates how sediments respond to chemical changes in pore fluids. Fig. 10 shows the measured data of montmorillonite and diatom samples in DW, brine, and kerosene under varying water content conditions in the liquid-plastic limit determination experiment.

Changes in pore fluid chemistry occur during hydrate formation, where each unit of CO_2 hydrate consumes 0.79 units of fresh water, increasing ion concentration in the brine (Jang and Santamarina, 2016). Continuous CO_2 injection prevents pore fluid from rebalancing to its initial salinity, causing sediments in low-ion environments to react to elevated ion concentrations (Jang et al., 2018). When particle size is below 1 μm or the specific surface area exceeds 25 m^2/g, electric forces dominate particle arrangement, reducing gravitational effects (Jang et al., 2018).

Additional, end-member particle clusters and fabrics influence settling behavior and interactions with coarse particles, forming frameworks or sealing units wrapped in hydrates, thus limiting hydrate exposure to pore fluid (Jang et al., 2018).

The electrical sensitivity and liquid limit are related to the induced nucleation and formation time of hydrates (as shown in Fig. 11). The relationship between electrical sensitivity and liquid limit, based on Jang and Santamarina (2016)'s study, confirms the repeatability of this experiment. Montmorillonite, with the highest electrical sensitivity, shows the shortest induction and formation times, followed by diatom, while glass beads exhibit the longest times, inversely proportional to electrical sensitivity. High electrical sensitivity in montmorillonite leads to excessive surface charges that influence pore fluid chemistry, facilitating CO_2 entry and increasing nucleation sites. However, in the later stages of hydrate formation, increased ion concentration reduces montmorillonite's permeability, hindering CO_2 diffusion. Diatom, with medium

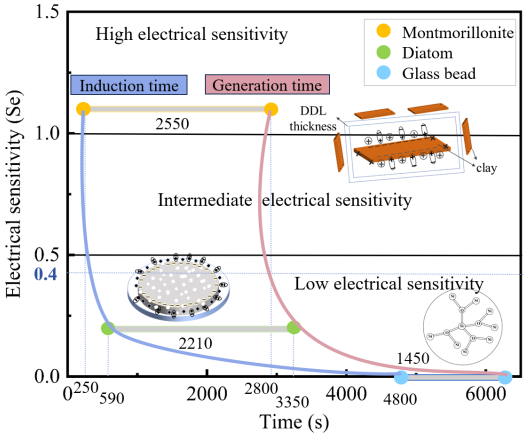

Fig. 11. Relationship between electrical sensitivity and the hydrate formation time of montmorillonite, diatom, and glass beads.

electrical sensitivity, has fewer surface ions and a thinner DDL, making it less sensitive to ion concentration changes and more effective in later stages. Thus, electrical sensitivity significantly impacts hydrate formation, and considering it in geological CO_2 storage can improve storage efficiency by selecting suitable locations.

In summary, significant differences exist in the hydrate formation characteristics among the three sediment types, including induction time, morphological evolution, temperature and pressure trends, gas consumption, hydrate conversion rate, and electrical sensitivity of the end-member sediments.

3.4 Impact on hydrate-based geological carbon sequestration

The experiments detailed above reveal that fine sediments, particularly montmorillonite, exerts a promotive effect on the nucleation process of hydrates, as illustrated in Tables 2 and 3. Clay minerals, such as montmorillonite, enhance their ability to provide many nucleation sites and increase the contact area with gas. Additionally, montmorillonite exhibits high electrical sensitivity, characterized by excessive unbalanced surface charges that make it highly responsive to changes in pore fluid chemistry. The surface electric field can further facilitate the nucleation of hydrates. As depicted in Fig. 7, during the later stages of hydrate generation, the formation conditions for hydrates in diatom become relatively mild, with montmorillonite's inhibitive effect becoming more pronounced. This inhibition arises because the large quantity of hydrates formed in the early stages impedes the mass transfer from the gas phase to the liquid phase, thus hindering further hydrate formation. Due to the response of the electrical sensitivity of diatom to the change of ion concentration, the stability of hydrate may be increased to a certain extent. Furthermore, Ren et al. (2022) demonstrated that clay can inhibit the decomposition of hydrates, necessitating more energy to induce their breakdown, and can serve a degree of anti-seepage function. Consequently, the presence of clay not only promotes the formation of hydrates, but also reduces the possibility of gas leakage due to hydrate decomposition, which is conducive to the storage of CO_2. The mechanism diagram is shown in Fig. 12.

4. Conclusions

This study investigates the impact of various end-member sediments on hydrate formation through dynamic experiments, morphological observations, and electrical sensitivity assessments. The key findings are summarized as follows:

1) Montmorillonite provides a large number of nucleation sites for hydrate due to its small particle diameter, large surface charge and clay-water migration. However, due to the difficulty of mass transfer and gas diffusion in the later stage, the formation rate of hydrate slows down. Diatom provide nucleation sites due to their unique hollow and porous structures, showing relatively mild phase conditions in the later stage of hydrate formation.
2) Morphological observations reveal that, in the early stages of hydrate formation, water migrates upwards along the reactor vessel wall due to surface tension. Hydrates preferentially form as a thin film at the gas-liquid interface, grow along the reactor wall, and eventually enter both the gas and liquid phases. However, excessive hydrate formation later in the reaction leads to mass transfer issues. Significant Ostwald ripening effects were noted in the glass bead group, accompanied by the appearance of free water and the formation of numerous new hydrates.
3) The induction time and complete reaction time of hydrates show an inverse relationship with the electrical sensitivity of the end-member sediments. Higher electrical sensitivity correlates with shorter induction and reaction times, suggesting that soil electrical sensitivity influences hydrate formation.

These experimental results elucidate the mechanisms by which soil with varying electrical sensitivities affects hydrate formation, thereby providing a foundational basis for developing scientifically informed carbon sequestration strategies.

Acknowledgements

This work was supported by the National Natural Science Foundation of China Youth Project (No. 42306234), the Jiangsu Basic Research Program Natural Science Foundation Youth Fund (No. SBK2023044900), and the General Projects of the National Natural Science Foundation of China (No. 52274061). Acknowledgments also go to the Changzhou University High-level Talent Introduction Program.

Conflict of interest

The authors declare no competing interest.

References

Alhammad, F., Ali, M., Yekeen, N. P., et al. Effect of methylene blue on wetting characteristics of quartz/H_2/brine

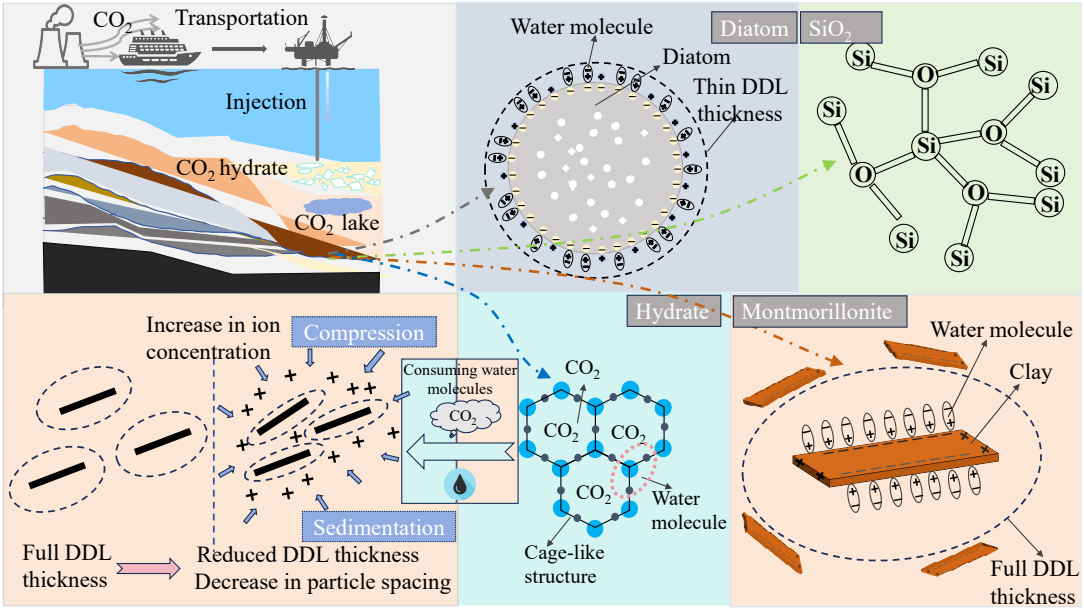

Fig. 12. End-member sediments reaction mechanism diagram of hydrate formation.

systems: Implication for hydrogen geological storage. Journal of Energy Storage, 2023, 72: 108340.

Alhammad, F., Ali, M., Yekeen, N. P., et al. The effect of methylene blue and organic acids on the wettability of sandstone formation: Implications for enhanced oil recovery. Capillarity, 2024, 10(2): 29-37.

Aminnaji, M., Qureshi, M. F., Dashti, H., et al. CO_2 gas hydrate for carbon capture and storage applications-Part 1. Energy, 2024, 300: 131579.

Bahk, J. J., Kim, D. H., Chun, J. H., et al. Gas hydrate occurrences and their relation to host sediment properties: Results from Second Ulleung Basin Gas Hydrate Drilling Expedition, East Sea. Marine and Petroleum Geology, 2013, 47: 21-29.

Bai, Y., Cao, G., An, H., et al. Generation laws and distribution characteristics of carbon dioxide hydrate in a reaction kettle. Experimental Thermal and Fluid Science, 2020, 116: 110125.

Bello-Palacios, A., Almenningen, S., Fotland, P., et al. Experimental and numerical analysis of the effects of clay content on CH_4 hydrate formation in sand. Energy & Fuels, 2021, 35(12): 9836-9846.

Bhattacharjee, G., Kumar, A., Sakpal, T., et al. Carbon dioxide sequestration: Influence of porous media on hydrate formation kinetics. ACS Sustainable Chemistry & Engineering, 2015, 3(6): 1205-1214.

Bowie, A. R., Maldonado, M. T., Frew, R. D., et al. The fate of added iron during a mesoscale fertilisation experiment in the Southern Ocean. Deep Sea Research Part II: Topical Studies in Oceanography, 2001, 48(11): 2703-2743.

Boyd, P. W., Abraham, E. R. Iron-mediated changes in phytoplankton photosynthetic competence during SOIREE. Deep Sea Research Part II: Topical Studies in Oceanography, 2001, 48(11): 2529-2550.

Buesseler, K. O., Andrews, J. E., Pike, S. M., et al. The effects of iron fertilization on carbon sequestration in the Southern Ocean. Science, 2004, 304(5669): 414-417.

Butler, J. A. V. Theory of the stability of lyophobic colloids. Nature, 1948, 162(4113): 315-316.

Cao, S. C., Jang, J., Jung, J., et al. 2D micromodel study of clogging behavior of fine-grained particles associated with gas hydrate production in NGHP-02 gas hydrate reservoir sediments. Marine and Petroleum Geology, 2019, 108: 714-730.

Cha, S. B., Ouar, H., Wildeman, T. R., et al. A third-surface effect on hydrate formation. The Journal of Physical Chemistry, 1988, 92(23): 6492-6494.

Chen, C., Zhang, Y., Li, X., et al. Investigations into methane hydrate formation, accumulation, and distribution in sediments with different contents of illite clay. Applied Energy, 2024, 359: 122661.

Chen, Y., Wang, H., Ji, S., et al. Toward high performance of zinc-air battery using hydrophobic carbon foam-based diffusion electrode. Journal of Industrial and Engineering Chemistry, 2019, 71: 284-292.

Chong, Z. R., Yang, M., Khoo, B. C., et al. Size effect of porous media on methane hydrate formation and dissociation in an excess gas environment. Industrial & Engineering Chemistry Research, 2016, 55(29): 7981-7991.

Derjaguin, B., Landau, L. Theory of the stability of strongly charged lyophobic sols and of the adhesion of strongly charged particles in solutions of electrolytes. Progress in Surface Science, 1993, 43(1): 30-59.

Doney, S. C., Busch, D. S., Cooley, S. R., et al. The impacts of ocean acidification on marine ecosystems and reliant human communities. Annual Review of Environment and Resources, 2020, 45: 83-112.

Eccles, J. K., Pratson, L. WITHDRAWN: Global CO_2 storage potential of self-sealing marine sedimentary strata.

Geophysical Research Letters, 2012, 39(24): 052291.

Feng, Y., Zhao, Y., Han, Y., et al. Formation and dissociation of CO_2 hydrates in porous media in the presence of clay suspensions. Chemical Engineering Journal, 2023, 465: 142854.

Ford, D. J., Shutler, J. D., Blanco-Sacristán, J., et al. Enhanced ocean CO_2 uptake due to near-surface temperature gradients. Nature Geoscience, 2024, 17(11): 1135-1140.

Giovannetti, R., Maria Gambelli, A., Castellani, B., et al. May sediments affect the inhibiting properties of NaCl on CH_4 and CO_2 hydrates formation an experimental report. Journal of Molecular Liquids, 2022, 359: 119300.

Gislason, S. R., Oelkers, E. H. Carbon storage in basalt. Science, 2014, 344(6182): 373-374.

Groos, A. F. K. v., Guggenheim, S. The stability of methane hydrate intercalates of montmorillonite and nontronite: Implications for carbon storage in ocean-floor environments. American Mineralogist, 2009, 94(2-3): 372-379.

Hassanpouryouzband, A., Yang, J., Tohidi, B., et al. Geological CO_2 capture and storage with flue gas hydrate formation in frozen and unfrozen sediments: Method development, real time-scale kinetic characteristics, efficiency, and clathrate structural transition. ACS Sustainable Chemistry & Engineering, 2019, 7(5): 5338-5345.

Hönisch, B., Ridgwell, A., Schmidt, D. N., et al. The geological record of ocean acidification. Science, 2012, 335(6072): 1058-1063.

Hubert, F., Caner, L., Meunier, A., et al. Unraveling complex <2 μm clay mineralogy from soils using X-ray diffraction profile modeling on particle-size sub-fractions: Implications for soil pedogenesis and reactivity. American Mineralogist, 2012, 97(2-3), 384-398.

IPCC, Climate Change 2007: Synthesis Report. Environmental Policy Collection, 2007, 27(2): 48.

Jang, J., Cao, S. C., Stern, L. A., et al. Impact of pore fluid chemistry on fine-grained sediment fabric and compressibility. Journal of Geophysical Research-Solid Earth, 2018, 123(7): 5495-5514.

Jang, J., Santamarina, J. C. Fines classification based on sensitivity to pore-fluid chemistry. Journal of Geotechnical and Geoenvironmental Engineering, 2016, 142(4): 06015018.

Jang, J., Santamarina, J. C. Closure to "fines classification based on sensitivity to pore-fluid chemistry" by Junbong Jang and J. Carlos Santamarina. Journal of Geotechnical and Geoenvironmental Engineering, 2017, 143(7): 07017013.

Jang, J., Waite, W. F., Stern, L. A., et al. Diatom influence on the production characteristics of hydrate-bearing sediments: Examples from Ulleung Basin, offshore South Korea. Marine and Petroleum Geology, 2022, 144: 105834.

Kong, D., Wu, H., Arulrajah, A. State-of-the-art review of geosynthetic clay liners. Sustainability, 2017, 9: 112110.

Kvamme, B., Aromada, S. A., Saeidi, N., et al. Hydrate nucleation, growth, and induction. ACS Omega, 2020, 5(6): 2603-2619.

Lamorena, R. B., Lee, W. Formation of carbon dioxide hydrate in soil and soil mineral suspensions with electrolytes. Environmental Science & Technology, 2008, 42(8): 2753-2759.

Lee, K. M., Lee, H., Lee, J., et al. CO_2 hydrate behavior in the deep ocean sediments; phase equilibrium, formation kinetics, and solubility. Geophysical Research Letters, 2002, 29(21): 30-1-30-4.

Li, J., Ye, J., Qin, X., et al. The first offshore natural gas hydrate production test in South China Sea. China Geology, 2018, 1(1): 5-16.

Li, Y., Chen, M., Song, H., et al. Effect of cations (Na^+, K^+, and Ca^{2+}) on methane hydrate formation on the external surface of montmorillonite: Insights from molecular dynamics simulation. ACS Earth and Space Chemistry, 2020, 4(4): 572-582.

Li, Y., Han, M., Wang, Z., et al. Molecular insights into the formation of carbon dioxide hydrates on the external surface of sodium montmorillonite in the presence of various types of organic matters. Gas Science and Engineering, 2024, 131: 205457.

Liu, J., Chen, M., Chen, Z., et al. Clay mineral distribution in surface sediments of the South China Sea and its significance for in sediment sources and transport. Chinese Journal of Oceanology and Limnology, 2010a, 28(2): 407-415.

Liu, P., Zhao, J., Li, Z., et al. Numerical simulation of multiphase multi-physics flow in underground reservoirs: Frontiers and challenges. Capillarity, 2024a, 12(3): 72-79.

Liu, Y., Li, Q., Lv, X., et al. The passive effect of clay particles on natural gas hydrate kinetic inhibitors. Energy, 2023, 267: 126581.

Liu, Z., Colin, C., Li, X., et al. Clay mineral distribution in surface sediments of the northeastern South China Sea and surrounding fluvial drainage basins: Source and transport. Marine Geology, 2010b, 277(1): 48-60.

Liu, Z., Liu, X., Yang, M., et al. Thermodynamic and kinetic properties of gas hydrate phase transition from formation to decomposition with applications: A review. Journal of Environmental Chemical Engineering, 2024b, 12(6): 114614.

Luckham, P. F., Rossi, S. The colloidal and rheological properties of bentonite suspensions. Advances in Colloid and Interface Science, 1999, 82(1): 43-92.

Luo, J., Xie, Y., Hou, M. Z., et al. Advances in subsea carbon dioxide utilization and storage. Energy Reviews, 2023, 2(1): 100016.

Ma, X., Jiang, D., Lu, J., et al. Hydrate formation and dissociation characteristics in clayey silt sediment. Journal of Natural Gas Science and Engineering, 2022, 100: 104475.

Martín-Puertas, C., Mata, M. P., Fernández-Puga, M. C., et al. A comparative mineralogical study of gas-related sediments of the Gulf of Cádiz. Geo-Marine Letters, 2007, 27(2): 223-235.

Mekala, P., Busch, M., Mech, D., et al. Effect of silica sand size on the formation kinetics of CO_2 hydrate in porous media in the presence of pure water and seawater relevant for CO_2 sequestration. Journal of Petroleum Science and Engineering, 2014, 122: 1-9.

Mojid, M. A., Cho, H. Estimating the fully developed diffuse

double layer thickness from the bulk electrical conductivity in clay. Applied Clay Science, 2006, 33(3): 278-286.

Pandey, G., Poothia, T., Kumar, A. Hydrate based carbon capture and sequestration (HBCCS): An innovative approach towards decarbonization. Applied Energy, 2022, 326: 119900.

Park, T., Kwon, T.-H. Effect of electric field on gas hydrate nucleation kinetics: Evidence for the enhanced kinetics of hydrate nucleation by negatively charged clay surfaces. Environmental Science & Technology, 2018, 52(5): 3267-3274.

Pecini, E. M., Avena, M. J. Measuring the isoelectric point of the edges of clay mineral particles: The case of montmorillonite. Langmuir, 2013, 29(48): 14926-14934.

Qureshi, M. F., Khandelwal, H., Usadi, A., et al. CO_2 hydrate stability in oceanic sediments under brine conditions. Energy, 2022, 256: 124625.

Ren, J., Liu, X., Niu, M., et al. Effect of sodium montmorillonite clay on the kinetics of CH_4 hydrate-implication for energy recovery. Chemical Engineering Journal, 2022, 437: 135368.

Ren, J., Zeng, S., Chen, D., et al. Roles of montmorillonite clay on the kinetics and morphology of CO_2 hydrate in hydrate-based CO_2 sequestration. Applied Energy, 2023, 340: 120997.

Schrag, D. P. Storage of carbon dioxide in offshore sediments. Science, 2009, 325(5948): 1658-1659.

Schroeder, A., Wiesner, M. G., Liu, Z. Fluxes of clay minerals in the South China Sea. Earth and Planetary Science Letters, 2015, 430: 30-42.

Shackelford, C. D. Fundamentals of soil behavior. Journal of Hazardous Materials, 2005, 125(1): 275-276.

Shi, S., Zhu, F., Feng, D., et al. Mechanical behaviors and elastoplastic damage constitutive model for heterogeneous frozen soil. Geomechanics for Energy and the Environment, 2023, 35: 100490.

Sridharan, A., Nagaraj, H. B. Compressibility behaviour of remoulded, fine-grained soils and correlation with index properties. Canadian Geotechnical Journal, 2000, 37(3): 712-722.

Sun, X., Shang, A., Wu, P., et al. A Review of CO_2 marine geological sequestration. Processes, 2023, 11(7): 072206.

Sun, Y., Jiang, S., Li, S., et al. Hydrate formation from clay bound water for CO_2 storage. Chemical Engineering Journal, 2021, 406: 126872.

Valle-Delgado, J. J., Molina-Bolívar, J. A., Galisteo-González, F., et al. Hydration forces between silica surfaces: Experimental data and predictions from different theories. The Journal of Chemical Physics, 2005, 123(3): 954747.

Wang, X., Zhang, F., Lipiński, W. Research progress and challenges in hydrate-based carbon dioxide capture applications. Applied Energy, 2020, 269: 114928.

Wang, Y., Chu, H., Lyu, X. Deep learning in CO_2 geological utilization and storage: Recent advances and perspectives. Advances in Geo-Energy Research, 2024, 13(3): 161-165.

Wei, N., Pei, J., Li, H., et al. Classification of natural gas hydrate resources: Review, application and prospect. Gas Science and Engineering, 2024, 124: 205269.

Wu, Z., Li, Y., Sun, X., et al. Experimental study on the gas phase permeability of montmorillonite sediments in the presence of hydrates. Marine and Petroleum Geology, 2018a, 91: 373-380.

Wu, Z., Li, Y., Sun, X., et al. Experimental study on the effect of methane hydrate decomposition on gas phase permeability of clayey sediments. Applied Energy, 2018b, 230: 1304-1310.

Xia, Y., Sai, X., Lu, C., et al. Characterization and capillary pressure curve estimation of clayey-silt sediment in gas hydrate reservoirs of the South China Sea. Advances in Geo-Energy Research, 2023, 10(3), 200-207.

Zhang, L., Sun, M., Sun, L., et al. In-situ observation for natural gas hydrate in porous medium: Water performance and formation characteristic. Magnetic Resonance Imaging, 2020, 65: 166-174.

Zhang, Z., Liu, L., Lu, W., et al. Permeability of hydrate-bearing fine-grained sediments: Research status, challenges and perspectives. Earth-Science Reviews, 2023, 244: 104517.

Zhao, J., Liu, Y., Yang, L., et al. Organics-Coated Nanoclays Further Promote Hydrate Formation Kinetics. The Journal of Physical Chemistry Letters, 2021, 12(13): 3464-3467.

Zhao, J., Zheng, J., Ren, L., et al. A review on geological storage of marine carbon dioxide: Challenges and prospects. Marine and Petroleum Geology, 2024, 163: 106757.

Zhou, S., Zhao, J., Li, Q., et al. Optimal design of the engineering parameters for the first global trial production of marine natural gas hydrates through solid fluidization. Natural Gas Industry B, 2018, 5(2): 118-131.